Journal of Materials Chemistry A

PAPER

View Article Online
View Journal | View Issue

Cite this: J. Mater. Chem. A, 2015, 3, 17165

MnO_2 nanoflake/polyaniline nanorod hybrid nanostructures on graphene paper for high-performance flexible supercapacitor electrodes†

Huailong Li,[a] Ying He,*[a] Vladimir Pavlinek,[b] Qilin Cheng,*[ab] Petr Saha[b] and Chunzhong Li[a]

Received 3rd June 2015
Accepted 15th July 2015

DOI: 10.1039/c5ta04008f

www.rsc.org/MaterialsA

A facile two-step strategy is adopted to construct a free-standing composite paper of MnO_2 nanoflake/polyaniline (PANI) nanorod hybrid nanostructures on reduced graphene oxide (RGO) for flexible supercapacitor electrode application. MnO_2 nanoflakes are first grown on RGO paper *via* an electrodeposition method, followed by assembly of PANI nanorods between MnO_2 nanoflakes by *in situ* polymerization using camphorsulfonic acid as a dopant. The morphology and structure of the composite paper are characterized and the electrochemical properties are systematically investigated. The interconnected PANI nanorods deposited on the interlaced MnO_2 nanoflakes have a length of ~100 nm and a diameter of ~30 nm, creating plenty of open porous structures which are beneficial for ion penetration into the electrode. The RGO/MnO_2/PANI composite paper shows a large specific capacitance of 636.5 F g^{-1} at 1.0 A g^{-1} in 1.0 M Na_2SO_4 electrolyte and excellent cycling stability (85% capacitance retention after 10^4 cycles). The optimized composite structure with more electroactive sites, fast ion and electron transfer, and strong structural integrity endows the ternary composite paper electrode with outstanding electrochemical performance.

Introduction

Nowadays, energy and environmental issues have become increasingly prominent due to the rapid growth of economy. To address these problems, considerable work has been devoted to searching renewable and clean energy as well as efficient energy storage and conversion technologies.[1–3] Supercapacitors (SCs), as one of the most important energy storage systems, have received a great deal of interest due to their large power density, fast charge–discharge rate and long cycling life and safety. Recently, flexible, lightweight and highly efficient energy devices have become very popular in modern markets. As such, flexible SCs have attracted significant attention due to their lightweight, small size, ease of handling, and high-flexibility,[4] as compared with conventional SCs. To date, much effort has been devoted to the design and preparation of flexible SCs, and significant progress has been made.[5–7] Nevertheless, the energy storage densities of flexible SCs still have to be further improved to meet their practical applications.

The performance of flexible SCs significantly depends on the structure and electrochemical activities of electrode materials. An ideal flexible electrode material should have good electrochemical properties, great mechanical strength upon bending or folding, and a balanced porous structure to adapt large strain without any loss of performance.[8] In this regard, carbon materials have brought substantial opportunities over the past few years for developing advanced flexible electrodes owing to their good conductivity, high surface area and favorable mechanical integrity.[9,10] In particular, graphene-based flexible electrodes have received intensive interest because of their excellent electrochemical stability, good structural, electrical and mechanical properties.[11] Recently, research in this field is focused on the synthesis of free-standing, binder-free and flexible electrodes by assembling individual RGO nanosheets into macroscopic RGO-based papers (or films).[12–14] However, the drawbacks during their processing are also obvious, that is, irreversible agglomeration and restacking of graphene nanosheets and low specific surface area of the paper (or film),[15] which inevitably lead to low specific capacitance and poor cycling stability of graphene-based paper electrodes.

One effective way to solve such problems is to assemble pseudocapacitive materials (*e.g.* conducting polymers and metal oxides) on RGO paper to construct high performance composite electrodes. The special synergistic effects between

[a]Key Laboratory for Ultrafine Materials of Ministry of Education, School of Materials Science and Engineering, East China University of Science and Technology, 200237 Shanghai, China. E-mail: rehey@ecust.edu.cn; chengql@ecust.edu.cn; Fax: +86-21-64253395; Tel: +86-21-64253395

[b]Centre of Polymer Systems, Tomas Bata University in Zlin, nam. T. G. Masaryka 5555, 760 01 Zlin, Czech Republic

† Electronic supplementary information (ESI) available. See DOI: 10.1039/c5ta04008f

RGO and pseudocapacitive materials may endow composite electrodes with high conductivity, large specific capacitance, and relatively high accessible surface area, and thus improve their energy density, power density, and cycling life. In such a case, various electroactive materials such as MnO_2,[8,16] Fe_3O_4,[17] PANI,[18,19] and polypyrrole[20] grown on RGO substrates for flexible SC applications have been developed. More recently, in order to obtain flexible electrodes with better electrochemical performance, the combination of the flexible substrate with two electroactive materials into a ternary composite system[21–23] has become a hot research spot. Of the pseudocapacitive materials, MnO_2 and PANI are the two most common classes of electrode materials for SC applications owing to their respective advantages in electrochemical activity. Therefore, it is naturally expected to achieve optimal performance by rationally designing RGO/MnO_2/PANI ternary composite electrodes. However, the great challenge here is to construct an optimum electrode architecture which not only provides a rich accessible active area for electrochemical reactions, but facilitates the kinetics of ion/electron transport throughout the electrode.

Herein, we develop a facile two-step strategy to design and fabricate a novel ternary composite by assembling MnO_2/PANI heterostructured nanocomposites on RGO paper for high performance flexible SCs. MnO_2 nanoflakes are first grown on RGO paper *via* an electrodeposition method and then PANI nanorods are embedded between intersecting MnO_2 nanoflakes by chemical oxidative polymerization. This unique nanoarchitecture ensures fast electron transfer, a short ion transport/diffusion path, and more electrochemical active sites. Based on the optimizing structure and fascinating synergistic effect between individual components, the flexible RGO/MnO_2/PANI composite paper electrode exhibits significantly enhanced electrochemical properties, such as much higher specific capacity (636.5 F g^{-1} at 1.0 A g^{-1}), superior cycling stability (85% capacitance retention after 10^4 cycles) and good rate capability.

Experimental

Materials

Hydroiodic acid (57 wt% in H_2O), the Anopore inorganic membrane (47 mm in diameter and 0.2 μm in pore size) and camphorsulfonic acid (CSA, 98%) were supplied by Sigma Aldrich. Graphite flakes (2–15 μm) were obtained from Alfa-Aesar company. Aniline bought from Shanghai Chemical Reagent Co. was distilled under vacuum before use. Ammonium persulfate (APS, 98%) and other chemicals were used as received.

Synthesis of RGO paper and RGO/MnO_2 nanoflake composite paper

GO was synthesized by a modified Hummers' method.[24] RGO paper was then obtained using hydroiodic acid (HI) as the reducing agent by the following procedure. First, 25 mg of GO was ultrasonically dispersed in distilled water (50 mL) for 2 h, followed by filtration to produce a GO paper. After drying in air, the GO paper was peeled from the filter and immersed into the hydroiodic acid (45%) at 85 °C for 3 h. Finally, the RGO paper was obtained by washing with distilled water and ethanol. The RGO/MnO_2 composite paper was prepared by electrodepositing MnO_2 on the RGO paper (1 × 2 cm^2). All electrodeposition experiments were performed on an Autolab PGSTAT-302N electrochemical workstation (Metrohm, Netherlands) with a standard three-electrode cell, where a RGO paper was used as the working electrode, and a platinum plate and an Ag/AgCl electrode were used as the counter electrode and reference electrode, respectively. The anodic electrodeposition of MnO_2 nanoflakes was performed in aqueous solution containing 0.1 M $Mn(CH_3COO)_2$ and 0.1 M Na_2SO_4 at a voltage of 0.8 V, and the deposition time was 5 min. Subsequently, the RGO/MnO_2 composite was washed with water and dried at 25 °C.

Synthesis of RGO/PANI and RGO/MnO_2/PANI composite paper

0.6 mL of aniline was injected into 40 mL of 0.1 M CSA solution, and 20 mL of 0.4 M APS solution was then rapidly added into the above solution under stirring. After being stirred vigorously for 2 min, the RGO paper and RGO/MnO_2 composite paper were dipped into the mixture respectively very carefully without stirring and kept for another 6 h at room temperature. After quick rinsing with water, the resultant RGO/PANI and RGO/MnO_2/PANI papers were placed in air overnight and then dried at 60 °C for 2 h under vacuum.

Materials characterization and electrochemical measurements

The morphology of the samples was investigated using a field-emission scanning electron microscope (FE-SEM, HITACHI S4800) and a transition electron microscope (TEM, JEOL 2100F). The specific surface area of samples was measured using the methylene blue adsorption method conducted on a UV-vis spectrometer (UNICO UV-2102PC) at room temperature. Raman spectra were measured on an Acton Raman spectrometer using a 531.4 nm laser as the excitation source. Fourier transformation infrared spectra (FTIR) of the samples were measured from KBr sample pellets on a Nicolet 5700 spectrometer. X-ray photoelectron spectroscopy (XPS) spectra were recorded on an AXIS Ultra DLD spectrometer (Kratos Analytical Ltd.) using a monochromatized Al Ka X-ray source (1486.71 eV). The electrochemical properties of the materials were measured by using a three-electrode cell in 1.0 M Na_2SO_4 electrolyte on an Autolab PGSTAT-302N electrochemical workstation at room temperature. The RGO paper or RGO-based composite paper was used as the working electrode, and an Ag/AgCl electrode and a platinum plate were used as reference and counter electrodes, respectively. Cyclic voltammetry (CV) and galvanostatic charge–discharge (GCD) curves were recorded from −0.1 to 0.9 V. The specific capacitance derived from GCD curves was derived from the discharged time in light of the following equation:

$$C = (I\Delta t)/(m\Delta V),$$

where I is the discharged current (A), Δt is the discharged time (s), m is the mass of the electroactive materials (g), and ΔV is the potential (V). Electrochemical impedance spectroscopy (EIS) was performed in the frequency range of 10^5 to 0.01 Hz.

Results and discussion

Fig. 1 depicts the two-step synthesis strategy of MnO_2/PANI hybrid nanostructures on RGO paper. First, MnO_2 nanoflake arrays were electrodeposited on the RGO paper within a mixed aqueous solution of $Mn(CH_3COO)_2$ and Na_2SO_4. Then PANI nanorods were grown onto the MnO_2 nanoflake backbone *via* an oxidative polymerization method assisted by the CSA dopant to form a hierarchically ternary composite. Both MnO_2 and PANI are employed as active materials, while the conductive RGO paper as a current collector guarantees effective ion and electron transport throughout the electrode.

The digital photographs in Fig. 2a show a free-standing RGO paper with dark-grey color. The obtained RGO paper exhibits high conductivity (14.5 Ω sq^{-1}) and light weight (1.35 mg cm^{-2}). After the growth of the MnO_2/PANI composite, the surface of the RGO paper becomes blue-green (inset of Fig. 2a). Both RGO paper and RGO-based composite paper are very flexible and bendable, as shown in Fig. 2a. The SEM image (Fig. 2b) of RGO paper indicates curved and wrinkled features on its surface, which are favourable for MnO_2 deposition. Fig. 2c further confirms that the RGO paper consists of densely layered sheets, which guarantee high flexibility and good mechanical strength of RGO paper. After a thin layer of the MnO_2/PANI composite is grown on RGO paper, the layered features of RGO and MnO_2/PANI with a one-dimensional nanostructure are clearly observed in Fig. 2d, where the MnO_2/PANI are well grown on the surface of RGO to form a tightly compact structure with a thickness of ~7.2 μm.

Fig. 3a shows the uniform growth of MnO_2 nanoflake arrays on the surface of RGO. The high-magnification SEM image (Fig. 3a, inset) reveals that the ultrathin nanoflakes are interlaced with each other and create abundant void spaces which ensure fast penetration of electrolyte ions into the inner side of electrode materials. It is worth noting that numerous

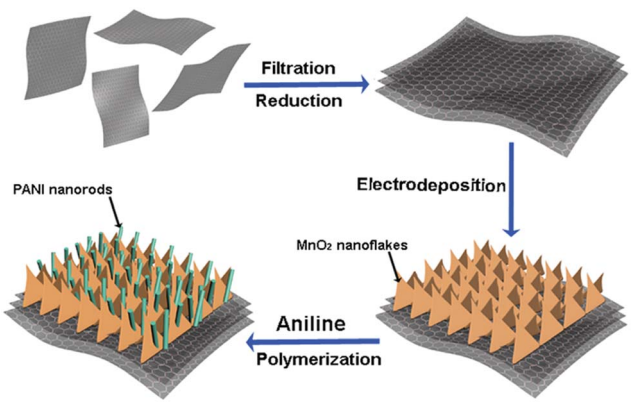

Fig. 1 Schematic illustration of the preparation process of the RGO/MnO_2/PANI nanocomposite.

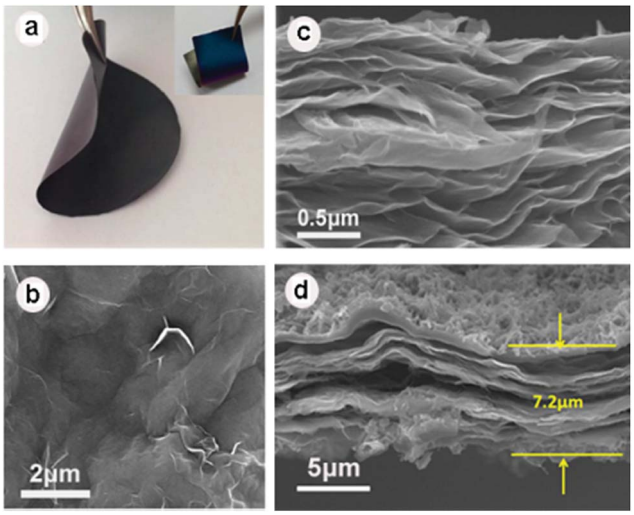

Fig. 2 (a) Digital images of RGO paper (the inset shows the digital image of RGO/MnO_2/PANI), SEM images of (b) RGO paper, (c) cross-sectional view of RGO paper and (d) cross-sectional view of RGO/MnO_2/PANI.

interconnected PANI nanorods are anchored on the MnO_2 skeletons by chemical polymerization of aniline, as evidenced by Fig. 3b. A high-resolution image (Fig. 3b, inset) indicates that the PANI nanorods with a length of ~100 nm and a diameter of ~30 nm are embedded into the space between MnO_2 nanoflakes without destroying the porous structures, which can benefit the transportation of the electrons and increase more electroactive surfaces. To further investigate the morphology of active materials on RGO paper, TEM images are also presented. Fig. 3c illustrates that the leaf-like ultrathin MnO_2 nanoflakes with a thickness of ~5 nm are deposited on the RGO paper, in good agreement with the SEM observation, while Fig. 3d demonstrates the presence of large amounts of rod-like PANI nanostructures on MnO_2 nanoflakes. In addition, the SEM image (Fig. S1†) of RGO/PANI paper indicates that PANI nanorods are grown aggregately on the RGO paper, which may reduce the utilization of PANI during the electrochemical reaction.

The specific surface areas of RGO, RGO/MnO_2, and RGO/MnO_2/PANI were measured to be 108.6, 87.1 and 78.1 m^2 g^{-1}, respectively. Although the specific surface areas of both composite papers decrease a little bit after the deposition of MnO_2 and MnO_2/PANI nanostructures, respectively, on the RGO paper, the values are comparable to those of other free-standing and flexible materials.

The existence of MnO_2 and PANI in the ternary composite can be confirmed by the FT-IR and Raman spectra (Fig. 4). The FT-IR spectrum of pristine RGO paper shows typical characteristic peaks of graphene. The strong peaks at 874, 1417, 2852 and 2925 cm^{-1} correspond to lateral vibrations of CH_2, deformation vibrations of C–OH, CH_2 symmetric and asymmetric stretching vibrations, respectively,[25] whereas, the weak peaks at 1064, 1247, and 1621 cm^{-1} are assigned to the C–O stretching vibrations of alkoxy and epoxy groups,[26] and skeletal

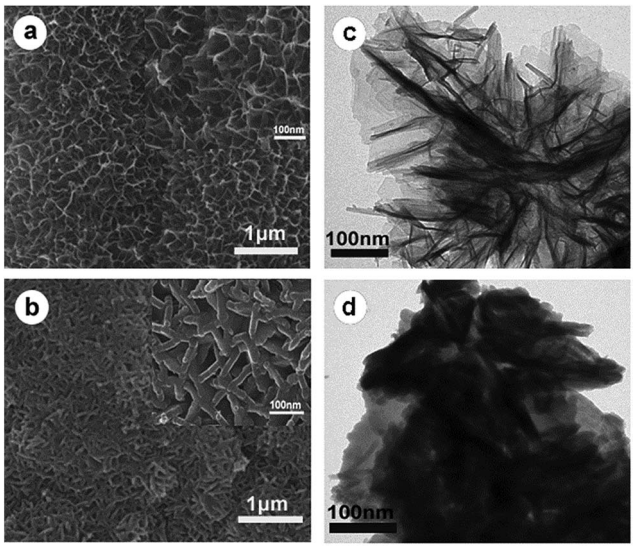

Fig. 3 SEM images of (a) RGO/MnO_2 and (b) RGO/MnO_2/PANI. TEM images of (c) MnO_2 nanoflakes and (d) MnO_2 nanoflakes/PANI nanorods. The insets in (a) and (b) show high-magnifications of respective SEM images.

vibration of graphene[27], respectively. In the case of RGO/MnO_2, the broad peak at ~3400 cm^{-1} is ascribed to the H–O–H bending of absorbed H_2O molecules. In addition, the peaks at 400–800 cm^{-1} are related to Mn–O stretching vibrations, indicating the presence of MnO_2 in the RGO/MnO_2 composite.[28] Meanwhile, the characteristic peaks of graphene are still observed except that the intensity is weakened due to the deposition of MnO_2 nanoflakes on the surface of RGO paper. As for the RGO/MnO_2/PANI composite, two typical peaks at 1490 and 1579 cm^{-1} represent the C=C stretching vibrations of the benzenoid and quinonoid rings, respectively. The other peaks at 819, 1148, 1237, and 1294 cm^{-1} correspond to the out-of-plane bending of C–H, in-plane bending of C–H, C=N stretching mode, and C–N stretching vibration, respectively.[29] These characteristic peaks are in agreement with the features of pure PANI, demonstrating the formation of PANI in the RGO/MnO_2/PANI composite. However, the peaks of MnO_2 and RGO become weak owing to the growth of PANI nanorod networks on RGO/MnO_2 composite paper. The appearance of PANI and MnO_2 in the ternary composite can also be verified by the Raman spectra (Fig. 4b). The RGO paper exhibits two distinct peaks at 1352 and 1591 cm^{-1} which are assigned to broad D and G bands, respectively. The high intensity of the D peak implies the presence of residual oxygen functional groups and other defects,[30] which is in accordance with the result of its FT-IR spectrum. A strong peak in the 480–680 cm^{-1} region is connected with the Mn–O stretching vibration,[28] indicating the presence of MnO_2 in the RGO/MnO_2 binary composite paper. In contrast, the curve of the RGO/MnO_2/PANI composite shows obvious peaks corresponding to PANI: the peaks at 1174 and 1565 cm^{-1} are related to the C–H bending and the C=C stretching of the quinoid ring, respectively. The peak at 1248 cm^{-1} is associated with the C–H bending of the benzenoid

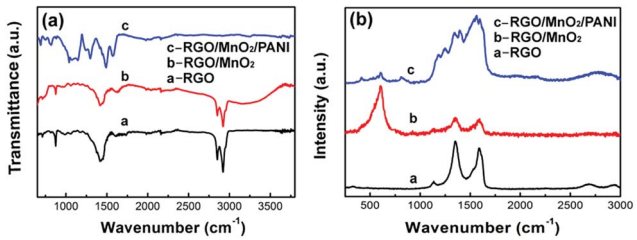

Fig. 4 (a) FT-IR spectra and (b) Raman spectra of RGO, RGO/MnO_2, and RGO/MnO_2/PANI.

ring, and the peak at 1342 cm^{-1} is attributed to the C–N^+ stretching vibration.[31] The weak or invisible peaks of MnO_2 and RGO in the Raman spectrum of RGO/MnO_2/PANI are caused by the masking effect of PANI.

Compositional analysis and the surface electronic state of the elements of RGO/MnO_2/PANI composite paper were examined by means of XPS (Fig. 5). The XPS spectra shown in Fig. 5a indicate the presence of C, N, O and Mn elements in the obtained ternary composite. Fig. 5b illustrates the XPS spectrum of C1s spectra which can be resolved into three peaks centered at 284.5 (C–C), 285.3 (C–N) and 286.5 (C–O).[32] The relatively weak signal of C–O reflects effective reduction of GO to RGO. For the N1s spectrum (Fig. 5c), the main peak is divided into three peaks corresponding to various electronic states: the nitrogen cationic radical at 400.1 eV ($N^{+\bullet}$), the quinoid amine at 399.5 eV and the benzenoid amine at 397.5 eV (–N=).[33] Based on the above-mentioned analysis, the doped state of PANI is formed in the composite. Fig. 5d presents the high-resolution Mn2p spectra, where the peaks at 642.05 and 653.85 eV with a spin energy separation of 11.8 eV correspond to $Mn2p_{3/2}$ and $Mn2p_{1/2}$, respectively, which is similar to those previously reported for MnO_2.[34,35]

To evaluate the electrochemical capacitive behavior of RGO/MnO_2 nanoflake/PANI nanorod ternary composite paper as a flexible and free-standing electrode for SCs, cyclic voltammetry (CV), galvanostatic charge/discharge (GCD) and

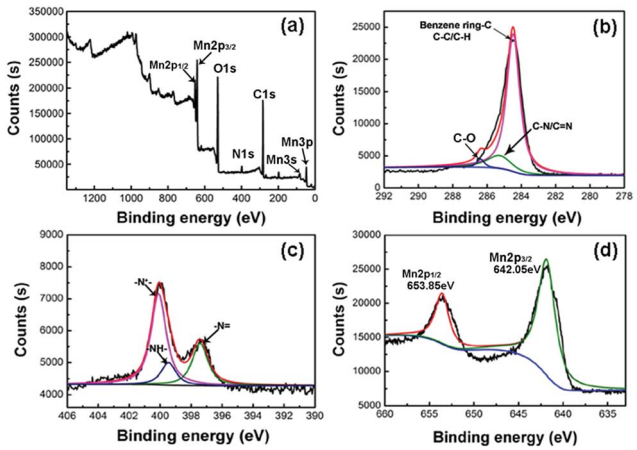

Fig. 5 (a) Wide scan survey XPS spectrum of RGO/MnO_2/PANI, (b) XPS C1s spectra of RGO/MnO_2/PANI, (c) XPS N1s spectra of RGO/MnO_2/PANI, and (d) XPS Mn2p spectra of RGO/MnO_2/PANI.

electrochemical impedance spectroscopy (EIS) were performed with a three-electrode system in 1.0 M Na_2SO_4 solution within a potential window of −0.1–0.9 V. As the hierarchical MnO_2/PANI nanostructures grown on the RGO, the RGO/MnO_2/PANI composite papers are expected to exhibit excellent performance as flexible SC electrode materials. In order to clarify the effect of the ratios of the three components on the specific capacitance, the ternary composites with various mass percentages of RGO, MnO_2 and PANI were measured by GCD at 1.0 A g^{-1} (Fig. S2a†), and the specific capacitances of the composites are plotted in Fig. S2b.† An appropriate ratio of the three components is important for the RGO/MnO_2/PANI composite with optimal performance. The composite with 52.7% RGO, 36.7% MnO_2 and 10.6% PANI possesses the maximum specific capacitance of 636.5 F g^{-1}. While the PANI content further increases beyond 17.3%, the capacitance of the composite decreases significantly. The excess PANI nanorods not only block up the open spaces in the composite but also reduce the active areas, which inevitably weaken the electrochemical performance of the ternary composite. Therefore, the mass percentage of RGO, MnO_2 and PANI in the RGO/MnO_2/PANI composite in our experiment is controlled at 52.7%, 36.7% and 10.6%, respectively.

Fig. 6a shows the CV curves of the RGO/MnO_2 composite paper measured at various scan rates. A pair of weak redox peaks can be observed in the CV curves at lower scan rates due to the reaction ($MnO_2 + Na^+ + e^- = MnOONa$) of MnO_2 in the composite electrode.[36] These CV curves are nearly rectangular, reflecting the good capacitive performance and excellent reversibility of RGO/MnO_2 composite paper electrodes. However, at higher scan rates (*e.g.* 100 mV s^{-1}), the CV profile deviates much from the rectangular shape and no evident redox peaks are observed. These phenomena are attributed to the polarization of the desolvation process of the hydrated sodium ions and relatively low conductivity of MnO_2 on RGO paper.[37] In comparison to the RGO/MnO_2 binary composite, the RGO/MnO_2/PANI ternary composite exhibits the characteristic quasi-rectangular shapes with perceptible redox peaks at all scan rates from 5 to 200 mV s^{-1} (Fig. 6b). This is because PANI nanorod networks embedded into the MnO_2 nanoflakes further improve the electrical conductivity of the composite and also increase the contact area between the electrode and electrolyte, which is favorable for charge transfer and ion transport.

Fig. 6c presents the GCD curves of the as-synthesized composite paper electrode. All the charge and discharge curves shown are nearly linear and symmetric at various current densities (1–50 A g^{-1}), and a fast *I–V* response implies good capacitive behavior of the RGO/MnO_2/PANI composite paper electrode. Even at a high current density of 50 A g^{-1}, the GCD curves are also close to symmetrical charge/discharge profiles with small deviations from linearity, suggesting fast diffusion of ions and low equivalent series resistance (ESR).[38] To further evaluate the role of MnO_2 and PANI, the CV curves of the RGO paper, RGO/MnO_2, RGO/PANI and RGO/MnO_2/PANI composite were measured at the same scan rate of 20 mV s^{-1}, as shown in Fig. 6d. The CV curve of pristine RGO paper is in rectangular shape, demonstrating ideal capacitive behavior based on electrical double layer charge storage. After the incorporation of

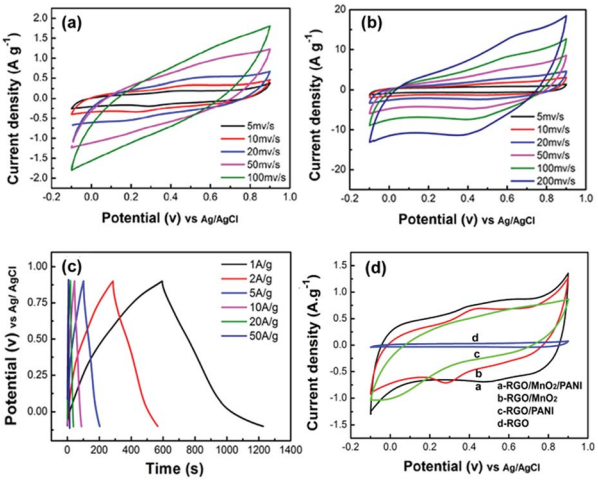

Fig. 6 CV curves of (a) RGO/MnO_2 and (b) RGO/MnO_2/PANI at different scan rates, (c) GCD profiles of RGO/MnO_2/PANI at various current densities, and (d) CV curves of RGO, RGO/PANI, RGO/MnO_2 and RGO/MnO_2/PANI at a scan rate of 20 mV s^{-1}.

MnO_2 nanoflakes, PANI nanorods and MnO_2/PANI nanostructures into the RGO substrate, respectively, binary and ternary composites show a much larger integrated area within the current–potential curves than RGO, indicating significantly improved capacitance due to the presence of MnO_2 and PANI pseudocapacitive materials. Moreover, the integrated area increases in the order of RGO < RGO/PANI < RGO/MnO_2 < RGO/MnO_2/PANI, demonstrating the higher specific capacitance of the ternary composite than that of the binary composite. The cross-linked PANI nanostructures embedded into the space between the MnO_2 nanoflakes not only reduce the internal resistance of the composite electrode and increase the active surface areas for pseudocapacitive reactions, but also provide a pathway for continuous charge transfer. In addition, PANI nanorods grown on the surface of MnO_2 nanoflakes can effectively restrain the MnO_2 particles from dissolution in the electrolyte and thus enhance electrochemical utilization. Therefore, the ternary composite possesses the highest specific capacitance among the three materials.

To further evaluate the contribution of the MnO_2/PANI hierarchical composite on RGO paper as a flexible electrode, the GCD curves of RGO, RGO/PANI, RGO/MnO_2, and RGO/MnO_2/PANI measured at a current density of 1.0 A g^{-1} are plotted in Fig. 7a. As expected, the RGO/MnO_2/PANI composite electrode possesses the longest discharge time, indicating the highest specific capacitance which is calculated to be 636.5 F g^{-1} at 1.0 A g^{-1}, much higher than that of RGO/MnO_2 (366.6 F g^{-1}), RGO/PANI (317.0 F g^{-1}) and pristine RGO paper (27.5 F g^{-1}). Moreover, this value is even larger than that of other MnO_2/PANI/graphene ternary composites.[28,39,40] The results further confirm that the ternary composite exhibits superior electrochemical performance due to the good synergistic effect between MnO_2 nanoflakes and PANI nanorods and the hierarchical assembly facilitating ion access into the composite interior. The changes of specific capacitance are also consistent with the result of their CV tests. Rate capability is also crucial to evaluate the power performance

of SCs, which can be determined by using the GCD technique at various current densities. Fig. 7b depicts the rate performance of both composite electrodes. It is evident that the RGO/MnO_2/PANI ternary composite yields significantly higher capacitance than the RGO/MnO_2 binary composite over the whole current density range. The capacitance retention of the RGO/MnO_2/PANI composite is 53.8% as the current density increases from 1.0 to 50 A g^{-1}, whereas that of RGO/MnO_2 and RGO/PANI is only 49.7% and 51.3%, respectively, under the same conditions.

The higher capacitance and better rate capability of the RGO/MnO_2/PANI composite are ascribed to the advantages of its unique structure. First, the PANI nanorods embedded into the interlaced MnO_2 nanoflakes not only increase the electroactive sites for a fast and reversible Faradaic reaction, but also create plenty of open spaces in the composite for easy penetration of the electrolyte into the electrode interior. Second, ultrathin MnO_2 nanoflakes and PANI nanorods with a small diameter can reduce the diffusion paths for electrons/ions and facilitate fast kinetics and high charge–discharge rates, ensuring the high utilization of MnO_2 and PANI. Third, the MnO_2/PANI hybrid nanostructures strongly adhere to the surface of RGO paper, avoiding the addition of conductive additives/polymer binders during the fabrication of electrodes, and thus enhancing the utilization of the electroactive material that contributes to the total capacitance and the rate capability.[21] Furthermore, the incorporation of nanometer-sized PANI into the composite increases the conductivity, reduces charge transfer resistance and enables fully ionic access, thus favoring higher capacitance. In addition, the RGO substrate serves as a conductive path to provide excellent interfacial contact for the MnO_2/PANI composite, and the strong synergistic effect between them also results in an enhanced electrochemical performance.

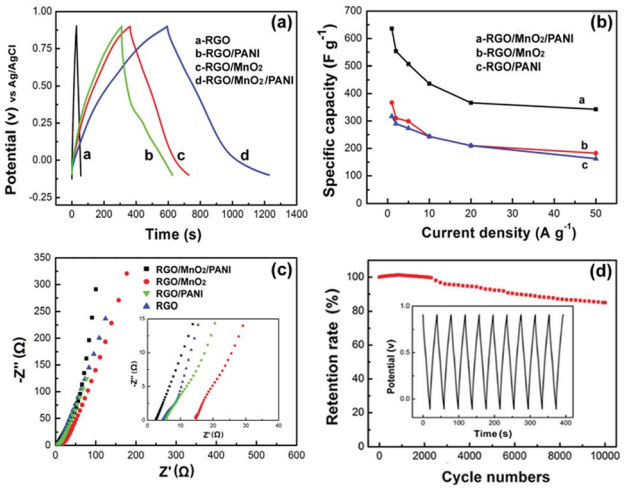

Fig. 7 (a) GCD profiles of RGO, RGO/PANI, RGO/MnO_2 and RGO/MnO_2/PANI at 1.0 A g^{-1}, (b) specific capacitances of RGO/PANI, RGO/MnO_2 and RGO/MnO_2/PANI at different current densities, (c) Nyquist plots of RGO, RGO/PANI, RGO/MnO_2 and RGO/MnO_2/PANI, the inset is the enlarged section of Nyquist plots in the high frequency region, and (d) cycling stability of RGO/MnO_2/PANI at a current density of 20 A g^{-1}, the inset shows the last 10 cycles of the charge–discharge curves.

In order to clarify the transport characteristics of the charge carriers within the ternary composite paper electrode, electrochemical impedance spectroscopy (EIS) was employed. The Nyquist plots of RGO, RGO/PANI, RGO/MnO_2 and RGO/MnO_2/PANI are given in Fig. 7c. In the low frequency region, all electrodes show a sloped line, indicating the capacitive behavior. The straight line of the RGO/MnO_2/PANI composite electrode is more vertical compared with the other samples, implying its better capacitive performance due to a faster ion diffusion rate of the electrolyte ions into this ternary composite electrode.[41] In the high frequency region (inset of Fig. 7c), the real axis intercept reflects the equivalent series resistance (R_e) which is related to the intrinsic resistance of the substrate, ionic resistance of the electrolyte and contact resistance between the active material and current collector.[42] The values of R_e from the Nyquist plots are 2.48, 14.9, 5.30 and 4.40 Ω for RGO/MnO_2/PANI, RGO/MnO_2, RGO/PANI and RGO, respectively. The lowest R_e value of the RGO/MnO_2/PANI composite electrode reflects that the conductivity and electroactivity of the composite are remarkably enhanced after the introduction of PANI nanorod networks. In addition, only the RGO/MnO_2/PANI composite electrode shows an invisible semicircle, demonstrating a very low charge-transfer resistance (R_{ct}) determined by the diameter of the semicircle in the high frequency region. A similar phenomenon can also be found for other PANI-based materials.[43,44] Hence, both the higher ion diffusion rate and lower charge-transfer resistance give rise to enhanced specific capacitance of the RGO/MnO_2/PANI composite.

Long-term cycling stability is another important aspect for evaluating the supercapacitor electrodes for practical applications. Fig. 7d illustrates the capacitance retention of the RGO/MnO_2/PANI composite electrode *versus* cycle number at a current density of 20 A g^{-1}. The capacitance retention is slightly over 100% during the first 500 cycles and then decreases gradually all the way, but still retains 85% after 10^4 cycles. The increased capacitance in the beginning can be interpreted as a result of the electrochemical activation commonly encountered in electrochemical processes.[45] Additionally, the stable charge and discharge curves for the last 10 cycles (inset of Fig. 7d) also confirm a good electrochemical stability of the RGO/MnO_2/PANI composite electrode. The good stability comes from the synergistic effect between MnO_2/PANI and RGO. The RGO paper acts as a robust substrate to immobilize active MnO_2/PANI hybrid nanostructures and endows the structural integrity of the hybrid composite on it, and therefore prevents the dissolution and loss of active materials due to the volume changes during the cycling process.[15] In addition, PANI nanorod networks formed between the MnO_2 nanoflakes also serve as a protection layer to prevent MnO_2 from dissolution into the electrolyte. Thus, the free-standing RGO/MnO_2/PANI composite paper with high capacitance, excellent rate capability and good cycling stability could be a promising electrode material for flexible SC applications.

Conclusions

Combining the efficient electro-deposition method and chemical oxidative polymerization, a flexible ternary composite of MnO_2 nanoflake/PANI nanorod hybrid nanostructures on RGO

paper has been successfully fabricated for binder-free supercapacitor electrode applications. Morphological and structural characterization studies indicate that the embedding of interconnected PANI nanorods into interlaced MnO_2 nanoflakes not only enhances the contact area between the active material and electrolyte but also facilitates the ion diffusion. The electrochemical analysis shows that the ternary composite material possesses a large specific capacitance of 636.5 F g^{-1} at 1.0 A g^{-1} and excellent rate capacity (53.8% retention at 50 A g^{-1}). In addition, the capacitance of RGO/MnO_2/PANI can retain 85% of the original value after 10^4 cycles at 20 A g^{-1}. The results provide a promising and effective way to develop high-performance flexible electrode materials for SCs.

Acknowledgements

This work was supported by the National Natural Science Foundation of China (21236003, 21371057, 21322607) and the Basic Research Program of Shanghai (13NM1400801, 13JC1401901).

Notes and references

1 B. D. Gate, *Science*, 2009, **323**, 1566–1567.
2 S. Bauer, *Nat. Mater.*, 2013, **12**, 871–872.
3 X. Wang, X. Lu, B. Liu, D. Chen, Y. Tong and G. Shen, *Adv. Mater.*, 2014, **26**, 4763–4782.
4 M. F. EI-Kady, V. Strong, S. Dubin and R. B. Kaner, *Science*, 2012, **335**, 1326–1330.
5 X. H. Lu, T. Zhai, X. H. Zhang, Y. Q. Shen, L. Y. Yuan, B. Hu, L. Gong, J. Chen, Y. H. Gao, J. Zhou, Y. X. Tong and Z. L. Wang, *Adv. Mater.*, 2012, **24**, 938–944.
6 Y. He, W. Chen, X. Li, Z. Zhang, J. Fu, C. Zhao and E. Xie, *ACS Nano*, 2013, **7**, 174–182.
7 L. F. Chen, Z. H. Huang, H. W. Liang, W. T. Yao, Z. Y. Yu and S. H. Yu, *Energy Environ. Sci.*, 2013, **6**, 3331–3338.
8 A. Sumboja, C. Y. Foo, X. Wang and P. S. Lee, *Adv. Mater.*, 2013, **25**, 2809–2815.
9 M. Kaempgen, C. K. Chan, J. Ma, Y. Cui and G. Gruner, *Nano Lett.*, 2009, **9**, 1872–1876.
10 B. G. Choi, J. Hong, W. H. Hong, P. T. Hammond and H. Park, *ACS Nano*, 2011, **5**, 7205–7213.
11 M. Pumera, *Chem. Soc. Rev.*, 2010, **39**, 4146–4157.
12 X. Yang, J. Zhu, L. Qiu and D. Li, *Adv. Mater.*, 2011, **23**, 2833–2835.
13 L. L. Zhang, X. Zhao, M. D. Stoller, Y. W. Zhu, H. X. Ji, S. Murali, Y. P. Wu, S. Perales, B. Clevenger and R. S. Ruoff, *Nano Lett.*, 2012, **12**, 1806–1812.
14 D. Sun, X. Yan, J. Lang and Q. Xue, *J. Power Sources*, 2013, **222**, 52–58.
15 K. Chi, Z. Zhang, J. Xi, Y. Huang, F. Xiao, S. Wang and Y. Liu, *ACS Appl. Mater. Interfaces*, 2014, **6**, 16312–16319.
16 Z. Li, Y. Mi, X. Liu, S. Liu, S. Yang and J. Wang, *J. Mater. Chem.*, 2011, **21**, 14706–14711.
17 M. Liu and J. Sun, *J. Mater. Chem. A*, 2014, **2**, 12068–12074.
18 H. P. Cong, X. C. Ren, P. Wang and S. H. Yu, *Energy Environ. Sci.*, 2013, **6**, 1185–1191.
19 H. Fan, N. Zhao, H. Wang, J. Xu and F. Pan, *J. Mater. Chem. A*, 2014, **2**, 12340–12347.
20 S. Li, C. Zhao, K. Shu, C. Wang, Z. Guo, G. G. Wallace and H. Liu, *Carbon*, 2014, **79**, 554–562.
21 L. Yu, G. Zhang, C. Yuan and X. W. Lou, *Chem. Commun.*, 2013, **49**, 137–139.
22 Y. Liu, Y. Jiao, B. Yin, S. Zhang, F. Qu and X. Wu, *J. Mater. Chem. A*, 2015, **3**, 3676–3682.
23 W. K. Chee, H. N. Lim, I. Harrison, K. F. Chong, Z. Zainal, C. H. Ng and N. M. Huang, *Electrochim. Acta*, 2015, **157**, 88–94.
24 N. I. Kovtyukhova, P. J. Ollivier, B. R. Martin, T. E. Mallouk, S. A. Chizhik, E. V. Buzaneva and A. D. Gorchinskiy, *Chem. Mater.*, 1999, **11**, 771.
25 M. R. Mahmoudian, Y. Alias and W. J. Basirun, *Electrochim. Acta*, 2012, **72**, 53–60.
26 D. K. Kampouris and C. E. Banks, *Chem. Commun.*, 2010, **46**, 8986–8988.
27 L. Ye and Z. Li, *Appl. Catal., B*, 2014, **160–161**, 552–557.
28 G. Wang, Q. Tang, H. Bao, X. Li and G. Wang, *J. Power Sources*, 2013, **241**, 231–238.
29 R. V. Salvatierra, M. M. Oliveira and A. J. G. Zarbin, *Chem. Mater.*, 2010, **22**, 5222–5234.
30 G. Eda, G. Fanchini and M. Chhowalla, *Nat. Nanotechnol.*, 2008, **3**, 270–274.
31 Y. Zhao, H. Bai, Y. Hu, Y. Li, L. Qu, S. Zhang and G. Shi, *J. Mater. Chem.*, 2011, **21**, 13978–13983.
32 H. L. Wang, Q. L. Hao, X. J. Yang, L. D. Lu and X. Wang, *Nanoscale*, 2010, **2**, 2164–2170.
33 O. Compton and S. Nguyen, *Small*, 2010, **6**, 711–723.
34 Z. S. Wu, W. Ren, D. W. Wang, F. Li, B. Liu and H. M. Chen, *ACS Nano*, 2010, **4**, 5835–5842.
35 G. R. Li, Z. P. Feng, Y. N. Ou, D. Wu, R. Fu and Y. X. Tong, *Langmuir*, 2010, **26**, 2209–2213.
36 J. Yan, E. Khoo, A. Sumboja and P. S. Lee, *ACS Nano*, 2010, **4**, 4247–4255.
37 Q. Qu, P. Zhang, B. Wang, Y. Chen, S. Tian, Y. Wu and R. Holze, *J. Phys. Chem. C*, 2009, **113**, 14020–14027.
38 S. Bose, T. Kuila, A. K. Mishra, R. Rajasekar, N. H. Kim and J. H. Lee, *J. Mater. Chem.*, 2012, **22**, 767–784.
39 P. Xiong, C. Hu, Y. Fan, W. Zhang, J. Zhu and X. Wang, *J. Power Sources*, 2014, **266**, 384–392.
40 G. Han, Y. Liu, L. Zhang, E. Kan, S. Zhang, J. Tang and W. Tang, *Sci. Rep.*, 2014, **4**, 4824.
41 J. G. Wang, Y. Yang, Z. H. Huang and F. Kang, *J. Mater. Chem.*, 2012, **22**, 16943–16949.
42 J. Gamby, P. L. Taberna, P. Simon, J. F. Fauvarque and M. Chesneau, *J. Power Sources*, 2001, **101**, 109–116.
43 K. Zhang, L. L. Zhang, X. S. Zhao and J. Wu, *Chem. Mater.*, 2010, **22**, 1392–1401.
44 G. P. Hao, F. Hippauf, M. Oschatz, F. M. Wisser, A. Leifert, W. Nickel, N. Mohamed-Noriega, Z. Zheng and S. Kaskel, *ACS Nano*, 2014, **8**, 7138–7146.
45 Y. T. Wu and C. C. Hu, *J. Electrochem. Soc.*, 2004, **151**, A2060–A2066.